Research Square

Preprints are preliminary reports that have not undergone peer review.
They should not be considered conclusive, used to inform clinical practice,
or referenced by the media as validated information.

Fabrication and Characterization of Functionally Graded MgB 2 Superconducting Wires via Integrated Powder Metallurgy and PIT Approaches

Salih Bilgin
Gazi University
Shanli Salahi
shanli.salahi@gmail.com

Gazi University
Berkay Çakır
Gazi University
Serap Safran
Ankara University, Superconductor Technologies Application and Research Center
Hanifi Çinici
Gazi University

Research Article

Keywords: MgB2 wire, Functionally Graded Materials, Powder Metallurgy, Activation Energy, Resistivity Measurement

Posted Date: November 12th, 2026

DOI: https://doi.org/10.21203/rs.3.rs-11270643/v1

License: This work is licensed under a Creative Commons Attribution 4.0 International License.
Read Full License

Additional Declarations: No competing interests reported.

Fabrication and Characterization of Functionally Graded MgB_2 Superconducting Wires via Integrated Powder Metallurgy and PIT Approaches

Salih Bilgin[1,2], Shanli Salahi[1*], Berkay Çakır[1], Serap Safran[3,4], Hanifi Çinici[1]

[1]*Gazi University, Department of Metallurgical and Materials Engineering, Ankara, Türkiye.*
[2]*Turkish Energy, Nuclear and Mineral Research Agency (TENMAK), Rare Earth Elements Research Institute (NATEN), Ankara, Türkiye.*
[3]*Ankara University, Superconductor Technologies Application and Research Center, Ankara, Türkiye.*
[4]*Ankara University, Science Faculty, Physics Department, Ankara, Türkiye.*

*Corresponding author: shanli.salahi@gmail.com

Abstract

In this study, functionally graded (FG) MgB_2 superconducting wire samples, with an external layer of 25 vol% B and 75 vol% Mg and an internal layer of 25 vol% Mg and 75 vol% B, were successfully synthesized via powder metallurgy by hot pressing at 400 MPa. Following the production step, the wire drawing process was performed, and the prepared samples were then subjected to sintering heat treatment at 700, 750, and 800 °C for 2, 4, and 6 h. X-ray Diffraction (XRD) analysis was conducted to confirm the formation of the hexagonal MgB_2 phase throughout the wire samples, along with minor secondary phases. Scanning Electron Microscopy (SEM) and Electrical Resistivity (R-T) analyses were performed to investigate the effects of heat treatment temperature and duration on the microstructure and superconducting characteristics of wire samples. The obtained results revealed that higher sintering heat treatment temperatures and longer durations improved phase homogeneity and grain connectivity, as well as the superconducting performance of the wire samples, due to the narrowest transition width observed. Furthermore, the calculated activation energy (E_a) values for the synthesized wire samples demonstrated the effect of heat treatment parameters on vortex pinning characteristics. The findings of this research revealed that optimized fabrication parameters of MgB_2 superconducting wire materials were achieved at a synthesis temperature of 800°C with a 2 h sintering duration, successfully balancing the phase homogeneity, grain connectivity, superconducting performance, and flux pinning efficiency.

Keywords: MgB_2 wire, Functionally Graded Materials, Powder Metallurgy, Activation Energy, Resistivity Measurement

1. Introduction

Magnesium diboride (MgB_2) is a superconductor discovered in early 2001 by Akimitsu et al. Since its discovery, it has become one of the most studied classes of materials; not only does it have unique properties but also a wide range of industrial applications **[1,2]**. MgB_2 compound is renowned for its simple intermetallic crystal structure, ease of synthesis, and lower production cost compared to high-temperature superconductors (HTS). In addition to advantageous physical and

chemical properties, it exhibits several notable features, including a relatively high critical transition temperature (T_c) among metallic superconductors, strong intergranular connectivity, large coherence length, lower anisotropy, suitable grain boundary properties, and a high critical current density (J_c) suitable for large-scale current transport **[3–5]**. Therefore, it is considered one of the most promising materials for commercial superconducting applications, with potential uses in maglev trains, magnetic resonance imaging (MRI), wind turbines, and related technologies **[6–9]**. For the numerous potential applications of superconductors, adopting novel fabrication methods and controlling parameters are understood to be as important as the superconducting properties. In this regard, numerous studies have been conducted to develop a suitable fabrication method and to enhance the superconducting effect by either optimizing the microstructure or refining the parameters **[5,10,11]**. Contemporary research on MgB2 conductors focuses on key parameters such as the irreversibility field (Hirr), Tc, and, subsequently, J_c versus magnetic field (B) **[8]**. However, MgB_2 wires produced by the powder-in-tube (PIT) method remain insufficient for practical applications due to their limited J_c **[12]**. One obstacle that gives rise to this issue is the significant porosity of the superconducting material, which results from the limited packing density of MgB_2 grains in the ex-situ method, as well as the shrinkage of the material that occurs during the reaction between boron (B) and magnesium (Mg) in the in-situ process. Additionally, the strong affinity of Mg for oxygen (O) leads to the prevalent formation of magnesium oxide (MgO) as a secondary phase in MgB_2 superconducting wires. The volume fraction and distribution of MgO affect the connectivity and pinning mechanisms in MgB_2 wires, making it crucial to control these parameters effectively **[13–15]**.

Moreover, continuous progress in manufacturing technologies has introduced a variety of methods, especially functionally graded materials (FGM), which have gained significant attention due to their ability to easily tailor mechanical and thermal properties **[16,17]**. Notably, recent advances in fabrication strategies have shown that transferring and adapting novel processing methods across different superconducting systems can yield significant improvements in material performance **[18–21]**. Techniques such as powder-in-tube (PIT) and other advanced sintering strategies have been successfully applied to MgB_2 superconductors, thereby enhancing microstructural homogeneity, improving grain connectivity, and substantially increasing J_c **[22–24]**. The Mg-B reaction would be the key to the improvement of the sintering efficiency as well as the superconducting properties. The sintering process with the flowing of argon (Ar) gas and the addition of Cu can lower the formation temperature of MgB_2 as low as 575 °C yet give a low critical temperature (~37 K) **[6,7]**. In order to preserve the high value of the critical temperature, an appropriate method needs to be developed. Parallel to this purpose, in the present research work, MgB_2 bulk samples were synthesized using the powder-in-tube (PIT) method by employing a FGM approach. Regarding the synthesis process of MgB_2, it is crucial to prevent the formation of the MgO phase.

In this work, a novel fabrication strategy based on FGM bulk structure design was employed for the first time for MgB_2 superconducting wire synthesis. Layered Mg and B powders with different internal and external compositions were prepared. With this novel approach, it was anticipated to enhance phase formation, reduce porosity and secondary detrimental phases, and improve both the superconducting transition and flux pinning behavior. The influence of sintering temperature and duration on phase evolution, structural integrity, and superconducting properties was investigated by performing XRD, SEM, Electrical Resistivity measurements (R-T, dR/dT), and flux pinning E_a calculations.

2. Materials and Methods

A novel Functionally Graded (FG) bulk design was employed to synthesize MgB_2 superconductors via the ex-situ Powder-in-Tube (PIT) technique utilizing a powder metallurgy route. High-purity commercial magnesium powder (99.5% purity, <325 µm, Sigma-Aldrich) and amorphous nano-sized boron powder (99.99% purity, <400 nm, PVZ) served as the precursor materials. The samples were engineered to exhibit a radial gradient in composition, consisting of two concentric zones designed to facilitate Mg diffusion during sintering. The architecture comprised an external layer rich in magnesium (75 vol% Mg + 25 vol% B) and an internal core rich in boron (25 vol% Mg + 75 vol% B), as illustrated in **Fig. 1**. The powder mixtures for each grade were homogenized separately using a 3D mixer (Turbula T2F) at 100 rpm for 60 minutes to ensure a uniform distribution of particles without inducing excessive mechanical alloying. Following the mixing phase, the powders were concentrically loaded into a cylindrical steel mold to form the FG structure. The assembly was subjected to a preheating stage at 300 °C for 1 h to remove volatile impurities. Subsequently, a hot-pressing process was applied at 400 MPa. This high-pressure compaction is critical for enhancing the initial green density of the bulk, which is a key factor in improving grain connectivity and critical current performance.

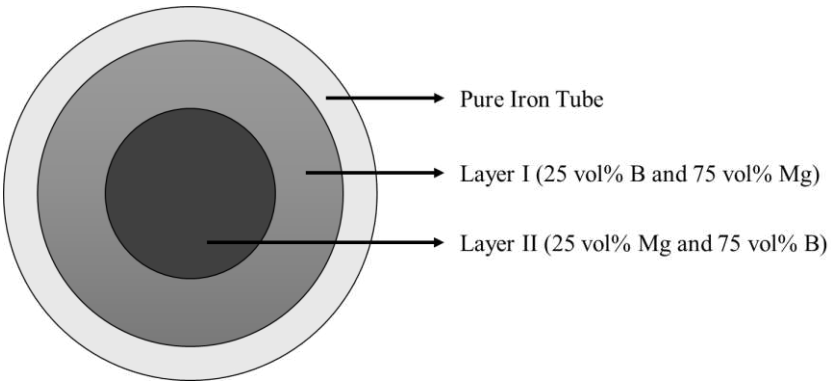


Fig. 1. FG structure of the fabricated MgB_2 wires.

The hot-pressed FG bulk cylinders were inserted into pure iron (Fe) tubes. Iron was selected as the sheath material due to its chemical inertness toward magnesium and boron, which prevents the formation of interfacial reaction layers that could degrade superconductivity. The composite tubes

were mechanically deformed by cold wire drawing to reduce the diameter to 2.5 mm, yielding wires approximately 110 cm in length. These wires were then sectioned into 10 cm segments and cleaned with ethanol to remove surface residues.

The final phase formation was achieved by sintering in a tubular furnace. To suppress Mg volatility and ensure stoichiometry conservation during the reaction, the process was conducted under a high-purity Argon atmosphere (99.99%) at a pressure of 10 bar. The samples were subjected to three sintering temperatures (700, 750, and 800 °C) for 2, 4, and 6 h, resulting in a matrix of nine experimental conditions (see **Table 1**). A heating ramp rate of 5 °C/min was maintained for all cycles, followed by furnace cooling to room temperature to minimize thermal residual stresses.

Table 1. Sample codes and heat treatment parameters of MgB_2 wires.

Sample ID	Sintering Temperature (°C)	Sintering Duration (h)
A2	700	2
A4	700	4
A6	700	6
B2	750	2
B4	750	4
B6	750	6
C2	800	2
C4	800	4
C6	800	6

The structural characterization of these synthesized MgB_2 samples was performed by X-ray diffraction (XRD) using a Rigaku Miniflex 2 diffractometer with CuK_α radiation (λ = 1.54 Å), operated at 30 kV and 15 mA. The diffraction data were collected over the 2θ range of 20–70 in steps of 0.02 with a scanning speed of 1 °/min. Microstructural analyses of the FG MgB_2 wire samples were conducted using a JEOL 6060 LV SEM at 20 kV. This examined the grain morphology, porosity, tube–core interface, and the integrity of the FG bulk structure, providing high-resolution surface imaging essential for evaluating microstructural homogeneity and overall structural quality. The density and porosity of the MgB_2 wire samples were assessed using the Archimedes method. The electrical resistivity of MgB_2 wires was measured using the four-probe contact method in a Janis CCS-450 brand closed-circuit cryostat. These measurements were conducted within a helium (He) gas circulation system in the temperature range of 20-45 K under a 0 to 7 T field.

3. Results and Discussion

3.1. Phase Identification and Structural Analysis

The XRD patterns of the MgB_2 wire samples are presented in **Fig. 2** to evaluate the structural crystallinity of the synthesized MgB_2 phase and secondary phases. **Fig. 2a** shows the standard JCPDS cards used for comparing the obtained diffraction peaks with standard reference data. In

Fig. 2b-d, information about peak comparison, phase composition, and crystal structures for A, B, and C sample groups is presented. The dominant diffraction peaks in all samples were indexed to the hexagonal MgB_2 phase (Space Group: P6/mmm), confirming the successful synthesis of the superconducting phase via the ex-situ PIT method coupled with the proposed FG design.

The characteristic diffraction peaks related to the MgB_2 phase were precisely observed in all synthesized wire samples, confirming the successful formation of this phase exhibiting superconducting properties. Furthermore, the obtained results demonstrate that MgB_2 has a hexagonal crystalline structure, with the most intense peaks detected in all wire samples at 2θ angle values of approximately 42°, 52°, and 60°, corresponding to (101), (002), and (110) planes, respectively. Alongside the main MgB_2 peaks, reflections corresponding to unreacted Mg and MgO secondary phases were also detected. The presence of residual metallic Mg is consistent with the initial stoichiometry, which was designed with excess Mg to compensate for potential losses during high-temperature sintering and to facilitate the liquid-state diffusion process. On the other hand, the observation of MgO peaks is attributed to the high oxygen affinity of magnesium powder. Since the precursor preparation was conducted in an ambient atmosphere, a certain degree of surface oxidation on the fine Mg powders was inevitable. While excessive MgO can act as a current blocker, distinct and dispersed MgO precipitates have also been reported to act as flux-pinning centers in some cases, potentially enhancing critical current density at higher magnetic fields **[13,25,26]**.

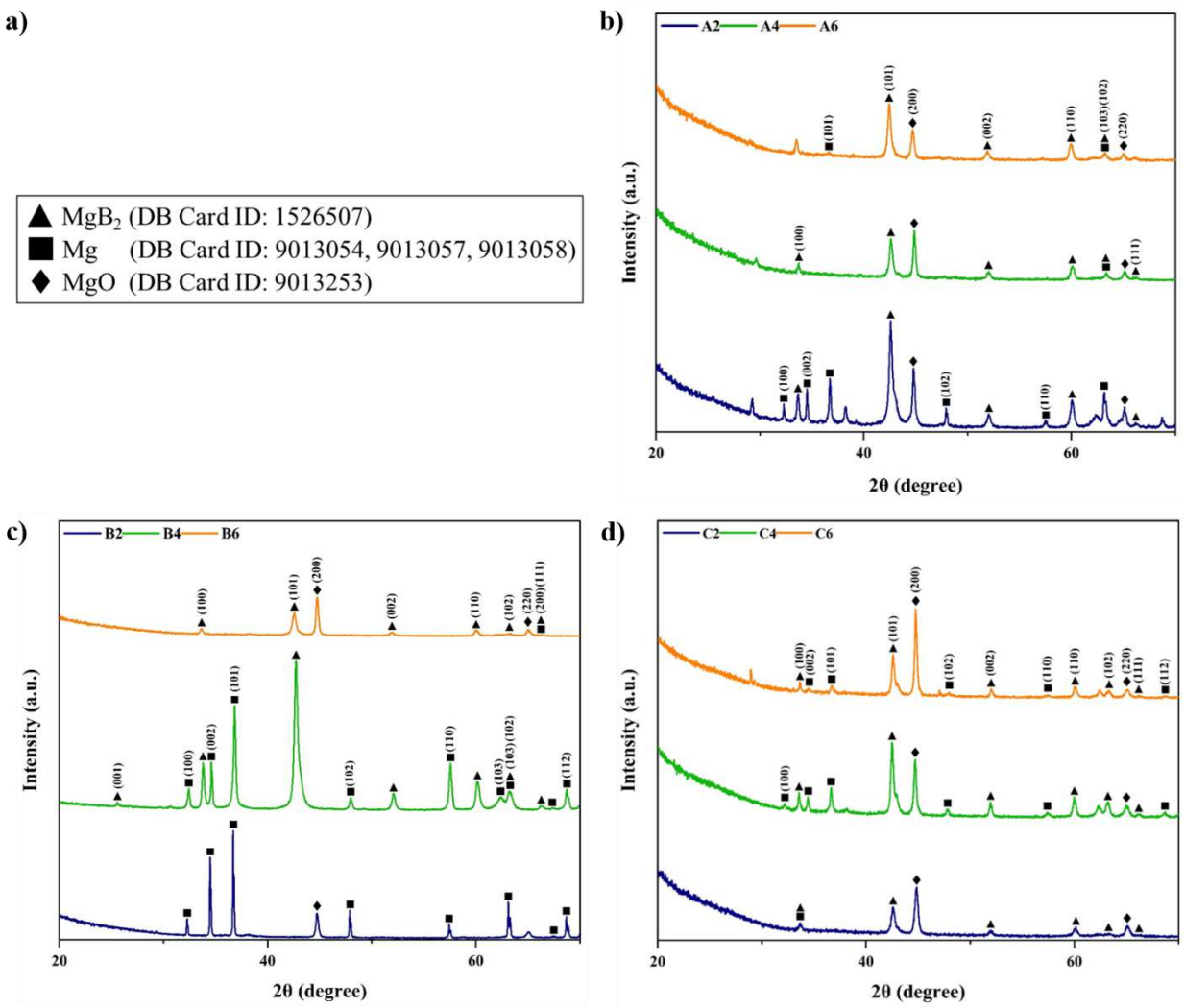


Fig. 2. a) Reference guide of identified phases and XRD graphs for samples sintered at **b)** 700 °C, **c)** 750 °C, and **d)** 800 °C.

The crystallite size and dislocation density of all wire samples were evaluated using Scherer's equation, as given in **Eqs. 1** and **2**. The θ and β (FWHM) values were obtained from Rigaku's standard DB XRD PDF Cards.

$$D = \frac{K\lambda}{\beta \cos\theta} \qquad \textbf{Eq. 1}$$

Where D represents the crystallite size, K is the Scherrer constant, λ denotes the X-ray wavelength, β corresponds to the FWHM, and θ is the peak angle. Dislocation density was calculated using **Eq. 2**, where δ represents the dislocation density. The calculated values of crystallite size and dislocation density of wire samples are given in **Table 2**.

$$\delta = \frac{1}{D^2} \qquad \textbf{Eq. 2}$$

Table 2. The crystallite size and dislocation density of MgB_2-cored wires.

Sample ID	Crystallite Size (nm)	Dislocation Density (nm^{-2}) × 10^{-3}
A2	27.53	1.32
A4	25.64	1.52
A6	26.46	1.43
B2	30.68	1.06
B4	28.54	1.23
B6	26.05	1.47
C2	23.28	1.85
C4	31.69	0.99
C6	33.60	0.88

Table 2 summarizes the calculated microstructural parameters, including crystallite size and dislocation density. The calculated dislocation densities show an inverse correlation with crystallite size (Eq. 2), suggesting that samples with finer grains retain a higher density of structural defects. These defects are crucial for the superconducting performance, as they can serve as effective pinning centers for magnetic flux vortices **[27–30].** This microstructural evolution is strongly dependent on the reaction kinetics dictated by the sintering temperature. At 700 °C (Series A), the temperature is just above the melting point of Mg (~650 °C) **[31]**. At this stage, the viscosity of liquid Mg is relatively high, and diffusion into the Boron matrix is slower, leading to a more gradual phase formation predominantly controlled by solid-liquid interface diffusion. As the temperature increases to 750 °C and 800 °C, the fluidity of molten Mg increases significantly. This facilitates rapid capillary infiltration into the boron-rich core of the FG design, thereby accelerating the overall reaction kinetics **[32].** This rapid nucleation and infiltration at 800 °C explain the trends observed in **Table 2**. When the sintering duration is kept short at 2 h (Sample C2), the highly reactive liquid Mg promotes the formation of a dense superconducting core while successfully retaining the finest crystallite size (23.28 nm) and the highest dislocation density (1.85 × 10^{-3} nm^{-2}). This fine-grained structure maximizes the defect landscape necessary for strong flux pinning. However, as the sintering time at 800 °C is extended to 6 h (Sample C6), the excessive thermal energy promotes significant grain growth (Ostwald ripening). Consequently, the crystallite size increases to 33.60 nm, and the dislocation density drops sharply to 0.88 × 10^{-3} nm^{-2}, reducing the number of effective pinning centers.

3.2. Cross-Sectional Analysis of Microstructure

In order to verify the kinetics of phase formation and structure development in the XRD studies, a cross-sectional microstructure of the FG wires was investigated through SEM. Instead of covering all variations, the microstructural study is confined to the study of only three specific samples, which demonstrate the kinetic development of the MgB_2 phase, the sluggish reaction stage (Sample A2: 700 °C for 2 h), the optimal sintering stage (Sample C2: 800 °C for 2 h), and the

over-sintered stage (Sample C6: 800 °C for 6 h). The corresponding cross-sectional SEM micrographs are presented in **Fig. 3 (a–c).**

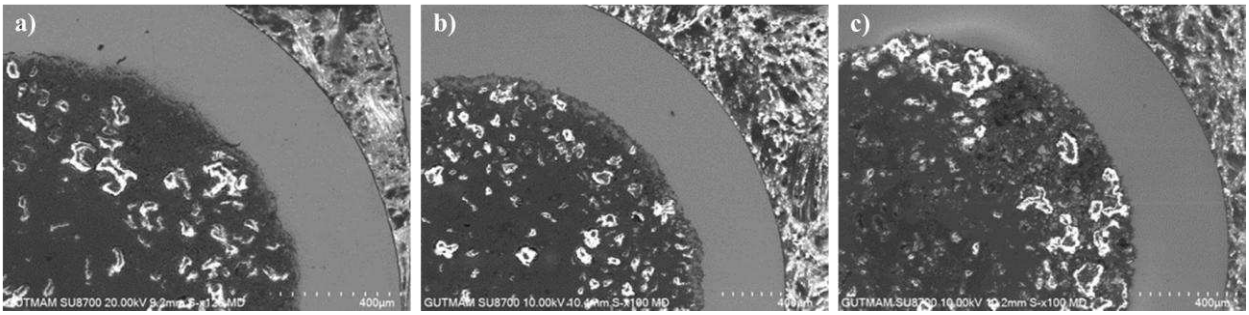


Fig. 3. SEM micrographs of phase transition regions of **a)** A2, **b)** C2, and **c)** C6 samples.

Fig. 3a displays the cross-section of Sample A2 sintered at 700 °C for 2 h. Although the sintering temperature is above the melting point of magnesium ($T_m \approx 650$ °C), the microstructure exhibits considerable porosity and loosely bonded particle clusters, particularly in the boron-rich core of the FG design. At 700 °C, the viscosity of the liquid Mg remains relatively high, restricting its capillary flow. Consequently, the infiltration of molten Mg into the dense boron matrix is incomplete within the 2 h window. This sluggish liquid-assisted diffusion fails to penetrate the inherent MgO layers on the precursor particles effectively. The resulting porous and weakly connected grain structure acts as a physical barrier to intergranular supercurrents, thereby directly explaining the poor field stability and rapid drop in E_a under applied magnetic fields in the A-series samples.

In contrast, increasing the temperature to 800 °C while maintaining the 2 h duration (Sample C2) yields a drastically improved morphological integrity, as shown in **Fig. 3b**. The interior region reveals a highly dense, coherent superconducting core with a significant reduction in macroscopic porosity. At 800 °C, the elevated thermal energy sharply decreases the viscosity of the molten Mg, significantly enhancing its fluidity. This low-viscosity liquid Mg rapidly infiltrates the interstices of the inner boron-rich layer, acting as a fast-transport medium that facilitates extensive intergranular fusion. The rapid reaction kinetics at this optimal window allow the formation of a robust percolative network before any significant grain growth can occur, successfully retaining the fine crystallite size (23.28 nm) observed in the XRD data. The clean and tightly packed grain boundaries observed in **Fig. 3b** serve as highly effective planar pinning centers, visually confirming why Sample C2 exhibits the sharpest superconducting transition (ΔT) and the highest flux pinning potential (E_a) at high magnetic fields.

The detrimental effects of extending the sintering time at high temperatures are clearly captured in the micrograph of Sample C6 (800 °C, 6 h), presented in **Fig. 3c**. Compared to the dense structure of C2, Sample C6 exhibits distinct signs of microstructural degradation. First, the individual MgB_2 grains appear noticeably coarsened, which is consistent with the Ostwald ripening

phenomenon driven by excessive thermal budgeting. This grain growth reduces the overall grain boundary area, thereby depleting the primary flux pinning centers. Furthermore, by exposing sample B to 800 °C for an extended period, Mg volatilizes to create large pores and dark cavities, as shown in Fig. 3c. This observation shows that the microstructure degrades in this manner. In fact, there is a perfect match between the high porosity of Sample C6 (13.16%) and over-sintering conditions. This porosity physically disrupts the continuous superconducting path, creating weak links that severely depress the intergranular connectivity. This visual evidence perfectly aligns with the earlier calculated drop in both the dislocation density and the E_a for the C6 sample. Ultimately, the SEM cross-sectional analysis provides compelling physical evidence that the 800 °C, 2 h parameter (Sample C2) represents a highly favorable processing window. It balances the need for rapid liquid-Mg infiltration to achieve high core density with the avoidance of grain coarsening and void formation associated with Mg volatility during over-sintering.

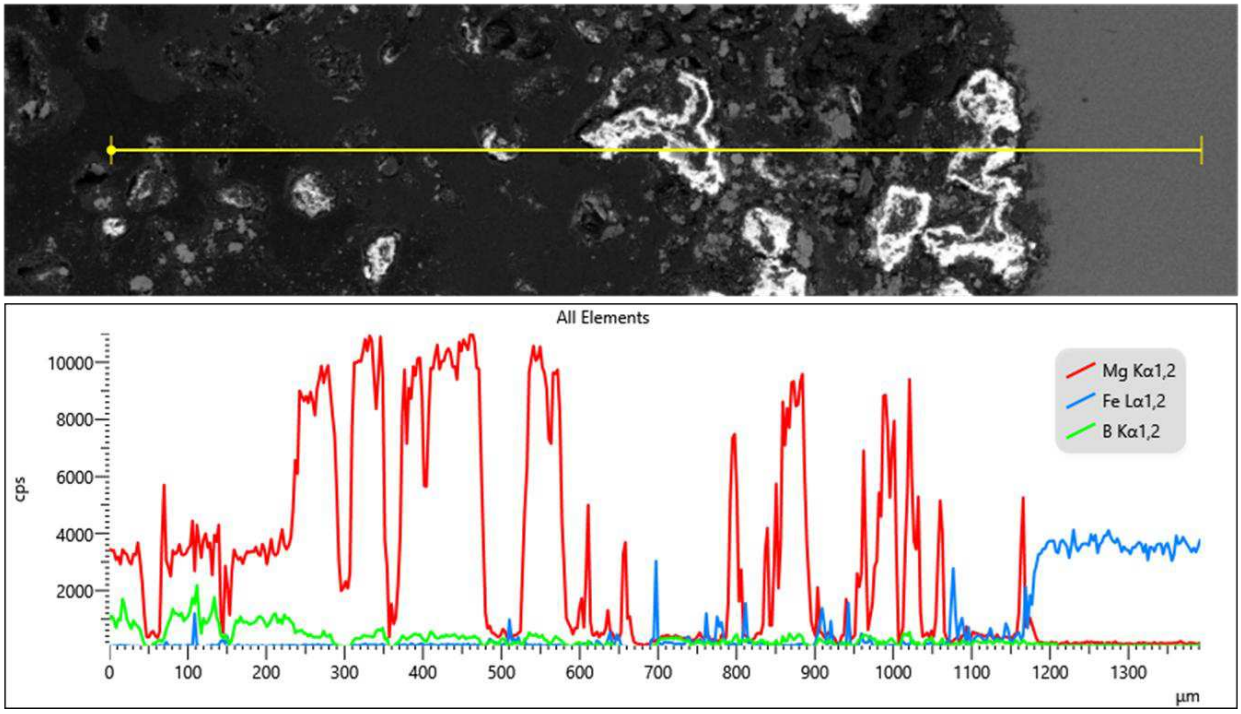


Fig. 4. Cross-sectional SEM image and EDS line analysis on the fabricated FG MgB_2 wire showing the distribution of Fe, Mg, and B elements in the Fe sheath, Mg-rich outer region (Layer I), and B-rich inner region (Layer II).

In **Fig. 4**, the SEM-EDS line scan applied to the cross-section of the fabricated FG MgB_2 wire is presented. The elemental diagram shows a designed three-layer composition in the fabricated wire. The external part of the wire shows a Fe peak, which corresponds to the pure iron sheath used in the PIT process. From the Fe sheath to the superconducting core, the line scan goes through Layer I, which has been intentionally designed as a Mg-rich layer (75 vol% Mg + 25 vol% B). Hence, the Mg peak is high, whereas the B peak is low in this layer. However, the elemental distribution starts changing from Layer I to Layer II, which is B-rich (75 vol% B + 25 vol% Mg). Thus, the B

intensity becomes relatively higher, whereas the Mg intensity becomes lower than that of Layer I. The relatively low B intensities over the scan can also be attributed to the relatively poor detection capability of EDS with respect to light elements like boron. However, the consistent occurrence and change of the B intensity, accompanied by the distribution of Mg, show the retention of the desired layered structure even after the wire drawing and sintering process. Eventually, when moving close to the opposite side, the Mg intensity falls dramatically, whereas the Fe intensity rises again, implying the transition from the superconducting core to the Fe sheath outside. Moreover, there was no noticeable Fe penetration into the Mg-B core, implying that no harmful interfacial reaction layer was formed during the sintering process and that the sheath material has good chemical compatibility. This compositional gradient should help diffuse Mg from the Mg-rich layer to the B-rich layer during the sintering process, which would lead to a better formation of the MgB_2 phase, higher grain connectivity, and thus result in the improvement of the superconducting properties of the fabricated FG MgB_2 wires.

3.3. Density and Porosity Analysis

The densification behavior of the superconducting wires is a critical factor determining the final critical current density (J_c), as porosity directly reduces the effective cross-sectional area for current flow. The porosity percentages (P %) were evaluated using the relation based on Archimedes' principle:

$$P(\%) = \frac{\rho_{Theo} - \rho_{Actual}}{\rho_{Theo}} \times 100 \qquad \textbf{Eq. 3}$$

Where ρ_{Actual} is the measured density of the sintered wire segments, and ρ_{Theo} represents the theoretical density of the fully dense composite wire. For the current configuration, ρ_{Theo} was calculated as 4.963 g/cm^3, accounting for the volume fractions of the Fe sheath and the stoichiometric MgB_2 core.

It is well established that the reactive formation of MgB_2 from elemental Mg and B precursors is accompanied by a theoretical volume contraction of approximately 25–30% **[25]**. Consequently, achieving a highly dense core relies predominantly on optimizing the sintering kinetics to facilitate the transport of liquid Mg into the interstitial voids of the boron matrix. As detailed in **Table 3**, the densification process is highly sensitive to the applied thermal budget. For the samples processed at 700 °C (Series A), densification exhibits a strong time dependency. Although 700 °C exceeds the melting point of Mg, the relatively high viscosity of the liquid phase impedes rapid capillary flow. Consequently, an extended sintering duration (6 h for Sample A6) is required to enable adequate liquid-assisted infiltration and particle rearrangement, resulting in a minimum porosity of 4.29% in this low-temperature series. Elevating the sintering temperature significantly accelerates the densification kinetics due to the enhanced fluidity of the molten Mg. The optimized sample C2 (800 °C, 2 h) exhibited a highly compact structure with low porosity, confirming that rapid infiltration of low-viscosity Mg effectively fills the precursor interstices before substantial grain coarsening can occur. However, a profound microstructural degradation is observed when the holding time is extended to 6 h at 800 °C (Sample C6), with the porosity abruptly increasing

to 13.16%. This retrograde densification behavior is a direct consequence of over-sintering. Prolonged thermal exposure induces severe Mg volatility, leading to the outward evaporation of Mg and the subsequent formation of large, isolated macroscopic voids, as previously corroborated by the SEM micrographs. Furthermore, concurrent Ostwald ripening (as evidenced by the increase in crystallite size in **Table 2**) isolates these newly formed pores within the expanding grains, rendering them extremely difficult to eliminate. This extensive porosity physically disrupts the inter-granular connectivity in sample C6, providing a clear volumetric explanation for the severe decline in its flux pinning potential and superconducting performance.

Table 3. Density and Porosity Rates of the wire MgB_2 samples

Sample ID	Density (g/cm^3)	Porosity Rate (%)
A2	4.256	14.23
A4	4.482	9.68
A6	4.750	4.29
B2	4.451	10.31
B4	4.705	5.19
B6	4.744	4.41
C2	4.715	4.99
C4	4.699	5.31
C6	4.309	13.16

3.4. Temperature dependence of the resistance

The superconducting transition characteristics of the FG MgB_2 wires were evaluated using temperature-dependent electrical resistivity (R−T) measurements at zero magnetic field. The normalized resistance (R/R_{max}) curves and their corresponding temperature derivatives (dR/dT) at zero field, grouped by sintering temperatures, are presented in **Fig. 5**. The critical parameters extracted from these measurements, including the onset critical temperature ($T_{c,\ onset}$) and the transition width ($\Delta T=T_{c,onset}-T_{c,offset}$), along with the high-field activation energies, are comprehensively summarized in a single unified table (**Table 4**).

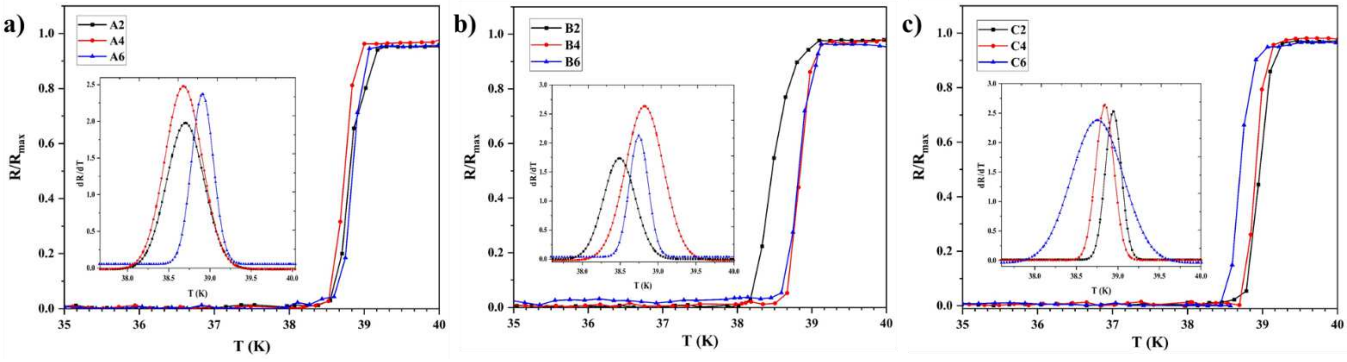


Fig. 5. R−T and dR/dT curves for **a)** A2, A4, and A6; **b)** B2, B4, and B6; **c)** C2, C4, and C6.

Inspection of the zero-field R−T data reveals that the $T_{c,onset}$ values for all fabricated samples fall within a remarkably narrow range of 39.0–39.7 K. Since $T_{c,onset}$ is an intrinsic property primarily governed by the intra-granular stoichiometry and crystal lattice integrity of the MgB_2 phase, this consistency indicates that the fundamental superconducting nature of the grains is well-preserved across all sintering conditions. However, a significant and systematic variation is observed in the ΔT, which is an extrinsic parameter strictly dictated by the grain boundary cleanliness, secondary phase inclusions, and overall inter-granular connectivity. The optimized sample C2 (800 °C − 2 h) exhibits the sharpest superconducting transition with a minimum ΔT of 0.68 K (as clearly seen in the narrow dR/dT peak in Fig. 6c). This exceptionally narrow transition width confirms that the rapid, low-viscosity liquid Mg infiltration at 800 °C not only achieved high core density but also successfully established a robust, percolative inter-granular network. The short sintering duration prevented excessive oxidation at the grain boundaries, effectively minimizing the weak-link behavior. Conversely, extending the sintering time at the identical temperature (Sample C6: 800 °C − 6 h) resulted in a substantial broadening of the transition, yielding a ΔT of 1.99 K. This nearly threefold increase in the transition width provides direct electrical evidence for the microstructural degradation discussed in the previous sections. The severe macroscopic porosity induced by Mg volatility, combined with the reduction of contact area due to Ostwald ripening, physically disrupts the continuous supercurrent paths. Consequently, these structural defects act as resistive barriers, retarding the global zero-resistance state ($T_{c,offset}$) and broadening the ΔT. For the low-temperature series (700 °C, Fig. 6a), the sluggish reaction kinetics predictably hindered the connectivity. Samples A2 and A6 exhibited broader transitions (ΔT=1.11 K and 1.52 K, respectively) compared to the optimal C2 wire. The relatively high viscosity of liquid Mg at 700 °C limited its capillary flow into the boron matrix, leaving unreacted voids and MgO-rich grain boundaries that impede phase coherence.

Table 4. Superconducting transition temperatures of $T_{c,onset}$, ΔT, and calculated E_a values for MgB_2 wire samples.

Sample	$T_{c,onset}$	ΔT	E_a *(kJ/mol)*			
	0 T	**0 T**	**1 T**	**3 T**	**5 T**	**7 T**
A2	39.29	1.11	116.73	19.70	10.82	7.49
A4	39.02	0.98	68.49	29.61	11.08	6.93
A6	39.37	1.52	91.57	31.41	16.40	6.64
B2	39.16	1.28	81.62	24.43	9.86	6.12
B4	39.71	1.75	66.22	18.26	12.43	4.80
B6	39.13	0.84	45.37	25.30	22.35	6.60
C2	39.28	0.68	107.46	37.27	14.43	9.10
C4	39.23	0.81	75.72	17.14	17.23	11.90
C6	39.74	1.99	71.58	14.78	12.39	6.59

To further investigate the robustness of the superconducting state, R−T measurements were conducted under varying external magnetic fields (1 to 7 T), as shown in **Fig. 6**. As the applied

magnetic field increases, the resistive transition curves of all samples shift toward lower temperatures and broaden significantly. This in-field broadening is a hallmark of Type-II superconductors, originating from the thermally activated motion of magnetic flux vortices (flux flow) driven by the Lorentz force. Notably, the degree of field-induced broadening is visibly less severe in Sample C2 compared to the A series and C6, implying a superior pinning landscape within the optimally sintered FG structure. The quantitative analysis of this flux pinning capability, evaluated through the thermally activated flux flow (TAFF) model and E_a calculations, is discussed in the following section.

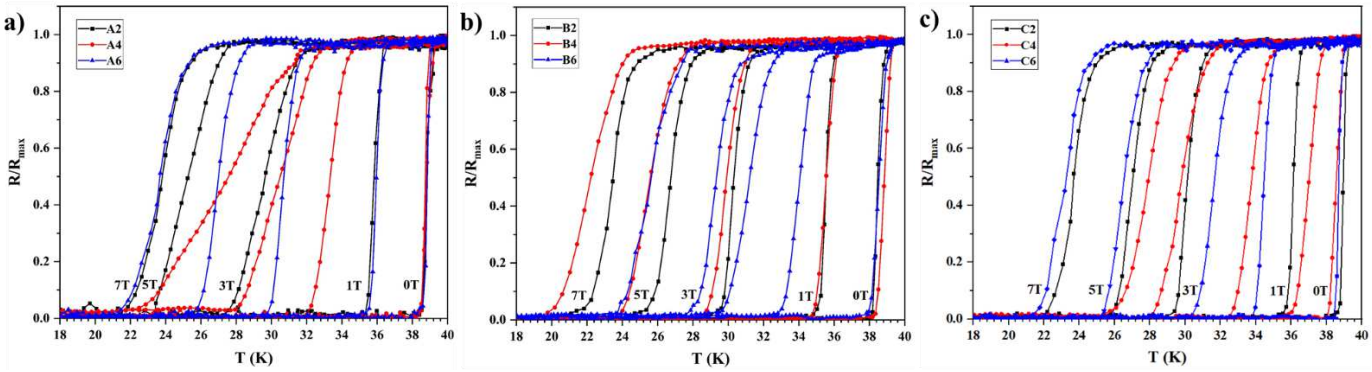


Fig. 6. R-T and dR/dT curves for **a)** A2, A4, and A6; **b)** B2, B4, and B6; **c)** C2, C4, and C6 under various magnetic fields.

3.5. Flux Pinning Mechanism and Activation Energy Analysis

The energy dissipation mechanism in the mixed state of the fabricated MgB_2 wires was analyzed using the Arrhenius relationship based on the Thermally Activated Flux Flow (TAFF) model. In Type-II superconductors, when an external magnetic field ($H>H_{c1}$) is applied, the broadening of the resistive transition is caused by the thermally activated motion of magnetic vortices driven by the Lorentz force. This motion is restricted by the pinning potential (U_0 or E_a), which represents the energy barrier that prevents the vortices from depinning. The resistivity $\rho(T,H)$ in this thermally activated regime is described by:

$$\rho(T,H) = \rho_0 \exp\left(-\frac{E_a(H)}{k_B T}\right) \qquad \textbf{Eq. 4}$$

Where ρ_0 is the field-independent pre-exponential factor, kB is the Boltzmann constant, and Ea(H) is the E_a for flux flow. It is crucial to note that E_a in this context refers strictly to the vortex depinning energy under magnetic fields, not to the intrinsic electronic band gap of the material. A higher E_a value indicates a stronger interaction between the flux lines and the microstructural pinning centers, such as grain boundaries. The E_a values were extracted from the slope of the linear region of the Arrhenius plots ($\ln\rho$ vs. 1/T). As presented in Table 4, the calculated in-field E_a values exhibit a strong dependence on the sintering kinetics.

At a low magnetic field of 1 T, Sample A2 exhibited the highest E_a of 116.73 kJ/mol, followed closely by the optimized Sample C2 with 107.46 kJ/mol. The unexpectedly high pinning potential in the sluggishly reacted sample (A2) can be attributed to its fine-grained microstructure, which provides a high density of grain boundaries acting as effective surface pinning centers. However, this pinning mechanism is extremely fragile against increasing magnetic fields due to the poor intergranular connectivity caused by the high-viscosity liquid Mg at 700 °C. As the field increased to 3 T, the E_a of Sample A2 dropped drastically to 19.70 kJ/mol (an ~83% reduction). Significantly, the enhanced field stability of the optimized FG design (Sample C2: 800 °C, 2 h) becomes evident at higher magnetic fields. In contrast to A2, Sample C2 maintained a notably higher value of 37.27 kJ/mol at 3 T. This robust field dependence proves that while finer grains provide strong pinning at low fields, the dense microstructure, optimum phase homogeneity, and clean grain boundaries achieved through rapid, low-viscosity liquid Mg infiltration in C2 are essential for sustaining supercurrents under higher magnetic fields.

Conversely, extending the sintering time to 6 h at 800 °C (Sample C6) resulted in a severe degradation of the pinning landscape, with its E_a dropping to 71.58 kJ/mol at 1 T. This reduction is a direct physical consequence of over-sintering. As previously confirmed by structural and morphological analyses, prolonged thermal exposure induces significant grain coarsening (Ostwald ripening), which drastically reduces the total grain boundary area per unit volume available for flux pinning. Furthermore, the macroscopic voids generated by Mg volatility physically disrupt the vortex pathways, creating weak links that suppress the global pinning potential. Therefore, the TAFF analysis conclusively demonstrates that the 800 °C–2 h parameter yields a highly favorable balance between effective grain-boundary pinning and optimal inter-granular connectivity, making it the most competitive processing window for the structurally graded MgB_2 wire design.

Conclusion

In this study, FG MgB2 superconducting wires, designed with a boron-rich inner core and a magnesium-rich outer layer, were successfully fabricated using the in-situ PIT method combined with integrated powder metallurgy. The investigation systematically evaluated how sintering kinetics (700–800 °C for 2–6 h) affect microstructural evolution, densification, and in-field superconducting properties of the wires. The principal findings are summarized as follows:

- Microstructural and volumetric analyses revealed that low-temperature sintering (700 °C) suffered from sluggish liquid-Mg infiltration due to its relatively high viscosity, resulting in a porous and weakly connected matrix. Increasing the temperature to 800 °C for a short duration (2 h; Sample C2) significantly enhanced the fluidity of molten Mg, thereby facilitating rapid capillary infiltration into the boron-rich core. This optimized kinetic window produced a highly dense microstructure while successfully retaining a fine crystallite size (23.28 nm) and a high dislocation density.

- Prolonged thermal exposure at 800 °C (6 h, Sample C6) led to a profound structural degradation. The excessive thermal budget triggered Ostwald ripening (grain coarsening), which reduced the effective grain boundary area. Concurrently, severe Mg volatility caused macroscopic void formation, drastically increasing the core porosity to 13.16% and physically disrupting the supercurrent pathways.
- Electrical transport measurements corroborated the structural observations. While the $T_{c,onset}$ remained highly stable (~39.0–39.7 K) across all specimens, ΔT varied significantly. Sample C2 exhibited the sharpest transition (ΔT=0.68 K), providing direct electrical evidence of superior intergranular connectivity and phase coherence, whereas the over-sintered C6 sample showed a substantially broadened transition (ΔT=1.99 K).
- TAFF analysis under applied magnetic fields demonstrated the vulnerability of poorly connected microstructures. Although the fine-grained A2 sample (700 °C, 2 h) exhibited high initial pinning at 1 T, its E_a values collapsed rapidly at 3 T (dropping to 19.70 kJ/mol). Conversely, the optimally infiltrated Sample C2 maintained a highly robust pinning potential (37.27 kJ/mol at 3 T). The over-sintered C6 sample exhibited a global depression in Ea due to the depletion of grain-boundary pinning centers.

Ultimately, this study establishes that the 800 °C–2 h parameter represents a highly favorable processing window for the FG wire architecture. It effectively balances the rapid liquid-Mg infiltration required for core densification with the retention of structural defects essential for robust flux pinning, thereby optimizing the performance of MgB_2 wires for practical magnetic field applications.

Declaration of Competing Interest

The authors declare that they have no known competing financial interests or personal relationships that could have appeared to influence the work reported in this paper.

Funding and Acknowledgment

No external funding was received for this research, and there are no acknowledgments to declare.

Credit Authorship Contribution Statement

Salih Bilgin: Investigation, Methodology, Data curation, Writing original draft – review & editing.
Shanli Salahi: Investigation, Validation, Visualization, Data curation, Writing original draft – review & editing.
Berkay Çakır: Investigation, Visualization, Data curation, Writing original draft – review & editing.
Serap Safran: Project administration, Supervision, Funding, Conceptualization, Methodology, Writing – review & editing.
Hanifi Çinici: Project administration, Supervision, Funding, Conceptualization, Methodology, Writing – review & editing.

References

[1] Y. Takano, H. Takeya, H. Fujii, H. Kumakura, T. Hatano, K. Togano, H. Kito, H. Ihara, Superconducting properties of MgB2 bulk materials prepared by high-pressure sintering, Appl. Phys. Lett. 78 (2001) 2914–2916. https://doi.org/10.1063/1.1371239.

[2] G. Simon, M. Miryala, Impact of doping on MgB2 superconductors: A comprehensive review, J. Alloy. Compd. Commun. 3 (2024) 100023. https://doi.org/10.1016/j.jacomc.2024.100023.

[3] C. Buzea, T. Yamashita, Review of the superconducting properties of MgB 2, Supercond. Sci. Technol. 14 (2001) R115–R146. https://doi.org/10.1088/0953-2048/14/11/201.

[4] C.C.T. Chow, M.D. Ainslie, K.T. Chau, High temperature superconducting rotating electrical machines: An overview, Energy Reports 9 (2023) 1124–1156. https://doi.org/10.1016/j.egyr.2022.11.173.

[5] D.C. Larbalestier, L.D. Cooley, M.O. Rikel, A.A. Polyanskii, J. Jiang, S. Patnaik, X.Y. Cai, D.M. Feldmann, A. Gurevich, A.A. Squitieri, M.T. Naus, C.B. Eom, E.E. Hellstrom, R.J. Cava, K.A. Regan, N. Rogado, M.A. Hayward, T. He, J.S. Slusky, P. Khalifah, K. Inumaru, M. Haas, Strongly linked current flow in polycrystalline forms of the superconductor MgB2, Nature 410 (2001) 186–189. https://doi.org/10.1038/35065559.

[6] S. Safran, Critical current density and mechanical performance of MgB2 superconductors prepared with different magnesium sources, Ceram. Int. 45 (2019) 10243–10249. https://doi.org/10.1016/j.ceramint.2019.02.077.

[7] S. Barua, M.S. Al Hossain, Z. Ma, D. Patel, M. Mustapic, M. Somer, S. Acar, I. Kokal, A. Morawski, T. Cetner, D. Gajda, S.X. Dou, Superior critical current density obtained in MgB2 bulks through low-cost carbon-encapsulated boron powder, Scr. Mater. 104 (2015) 37–40. https://doi.org/10.1016/j.scriptamat.2015.04.003.

[8] B.A. Glowacki, M. Majoros, M. Eisterer, S. Toenies, H.W. Weber, M. Fukutomi, K. Komori, K. Togano, MgB2 superconductors for applications, Phys. C Supercond. 387 (2003) 153–161. https://doi.org/10.1016/S0921-4534(03)00662-2.

[9] M. Maeda, D. Uchiyama, M.S. Al Hossain, Z. Ma, M. Shahabuddin, J.H. Kim, Control of core structure in MgB2 wire through tailoring boron powder, J. Alloys Compd. 636 (2015) 29–33. https://doi.org/10.1016/j.jallcom.2015.02.151.

[10] S. Herbirowo, E. Priyanto Utomo, D. Feronika Tinambunan, P. Sinuhaji, N. Sofyan, A. Herman Yuwono, A. Imaduddin, Properties of low-cost MgB2 superconducting wires fabricated by high reduction cold rolling, Mater. Today Proc. (2023). https://doi.org/10.1016/j.matpr.2023.01.250.

[11] J.S. Hansdah, P.M. Sarun, K. Asokan, Effect of carbon ion implantation on the superconducting properties of MgB2 bulks prepared by powder-in-sealed-tube method, Cryogenics (Guildf). 145 (2025) 103994. https://doi.org/10.1016/j.cryogenics.2024.103994.

[12] E.W. Collings, M.D. Sumption, M. Bhatia, M.A. Susner, S.D. Bohnenstiehl, Prospects for improving the intrinsic and extrinsic properties of magnesium diboride superconducting

strands, Supercond. Sci. Technol. 21 (2008) 103001. https://doi.org/10.1088/0953-2048/21/10/103001.

[13] A. Rosová, I. Hušek, P. Kováč, E. Dobročka, T. Melišek, Microstructure of MgB2 superconducting wire prepared by internal magnesium diffusion process, J. Alloys Compd. 619 (2015) 726–732. https://doi.org/10.1016/j.jallcom.2014.08.180.

[14] P. Kováč, M. Kulich, W. Haessler, M. Hermann, T. Melišek, M. Reissner, Properties of MgB2 wires made of oxidized powders, Phys. C Supercond. 477 (2012) 20–23. https://doi.org/10.1016/j.physc.2012.02.026.

[15] A. Kario, W. Hasler, M. Herrmann, C. Rodig, J. Scheiter, B. Holzapfel, L. Schultz, S. Schlachter, B. Ringsdorf, W. Goldacker, A. Morawski, Properties of ${\rm MgB}_{2}$ Tapes Prepared by Using MA In-Ex Situ Powder, IEEE Trans. Appl. Supercond. 20 (2010) 1521–1523. https://doi.org/10.1109/TASC.2009.2039777.

[16] M.W. Harmel, K. Zouggar, M. Jalalvand, B.B. Bouiadjra, R. Mhamdia, M. Baghdadi, Numerical damage analysis using FGA-USDFLD based on functionally graded cohesive zone modeling concept for bonded composite patch repairs, Int. J. Adhes. Adhes. 143 (2025) 104137. https://doi.org/10.1016/j.ijadhadh.2025.104137.

[17] S. Chakraborty, T. Dey, J. Jiang, M. Amabili, Influence of non-uniform temperature gradient on thermal post-buckling and vibration response of bi-directional functional graded composite plates, Compos. Struct. 371 (2025) 119526. https://doi.org/10.1016/j.compstruct.2025.119526.

[18] T. Spina, A. Ansaldo, A. Tumino, M. Paola, S. Pasini, C.E. Bruzek, M. Tropeano, G. Grasso, Recent Development and Status of Ex-Situ PIT MgB 2 Wires at ASG Superconductors, IEEE Trans. Appl. Supercond. 34 (2024) 1–4. https://doi.org/10.1109/TASC.2024.3353144.

[19] H. Kumakura, Resent Progress on MgB 2 Wires, IEEE Trans. Appl. Supercond. 35 (2025) 1–7. https://doi.org/10.1109/TASC.2024.3518463.

[20] A. Athanasiou-Ioannou, I.D. Theodorakopoulos, Improving the Characteristics of Powder-In-Tube MgB2 Superconductor Fabricated Using the Extrusion Technique, J. Supercond. Nov. Magn. 27 (2014) 1041–1047. https://doi.org/10.1007/s10948-013-2400-4.

[21] Z. Lei, C. Yao, W. Guo, D. Wang, Y. Ma, Progress on the Fabrication of Superconducting Wires and Tapes via Hot Isostatic Pressing, Materials (Basel). 16 (2023) 1786. https://doi.org/10.3390/ma16051786.

[22] N. Varghese, K. Vinod, A. Rao, Y.K. Kuo, U. Syamaprasad, Enhanced superconducting properties of bulk MgB2 prepared by in situ Powder-In-Sealed-Tube method, J. Alloys Compd. 470 (2009) 63–66. https://doi.org/10.1016/j.jallcom.2008.03.056.

[23] S.D. Yudanto, A. Imaduddin, B. Kurniawan, A. Manaf, Phase Evolution and Critical Temperature of MgB2 Superconductor Made of β-Rhombohedral Boron with Temperature Sintering Variation, Key Eng. Mater. 855 (2020) 215–220. https://doi.org/10.4028/www.scientific.net/KEM.855.215.

[24] D. Patel, A. Matsumoto, H. Kumakura, T. Moronaga, Y. Hara, T. Hara, M. Maeda, M.S.A.

Hossain, Y. Yamauchi, S. Choi, J.H. Kim, Superconducting Joining Concept for Internal Magnesium Diffusion-Processed Magnesium Diboride Wires, ACS Appl. Mater. Interfaces 13 (2021) 3349–3357. https://doi.org/10.1021/acsami.0c17385.

[25] Y. Liu, F. Cheng, Q. Cai, W. Qiu, Y. Lu, Z. Ma, The kinetics mechanism of MgB2 layer formation within MgB2 superconducting wire fabricated using improved internal Mg diffusion process, J. Alloys Compd. 697 (2017) 37–42. https://doi.org/10.1016/j.jallcom.2016.12.133.

[26] E. Aksu, Study of MgB2 phase formation by using XRD, SEM, thermal and magnetic measurements, J. Alloys Compd. 552 (2013) 376–381. https://doi.org/10.1016/j.jallcom.2012.11.088.

[27] J. Lee, J. Jeong, H. Lee, J. Park, J. Jang, H. Jeong, Effects of Sintering Processes on Microstructure Evolution, Crystallite, and Grain Growth of MoO2 Powder, Crystals 13 (2023) 1311. https://doi.org/10.3390/cryst13091311.

[28] S. Jeon, X. Liu, C. Azersky, J. Ren, S. Zhang, W. Chen, R.W. Hyers, K. Costa, M. Kolbe, D.M. Matson, Particle size effects on dislocation density, microstructure, and phase transformation for high-entropy alloy powders, Materialia 18 (2021) 101161. https://doi.org/10.1016/j.mtla.2021.101161.

[29] D. Gajda, A.J. Zaleski, A.J. Morawski, M. Małecka, L.M. Tran, M. Rindfleisch, T. Durejko, T. Czujko, High Critical Current Density in the Textured Nanofiber Structure in Multifilament MgB2 Wires Made by the Powder-In-Tube (PIT) Technique, Materials (Basel). 15 (2022) 5419. https://doi.org/10.3390/ma15155419.

[30] H. Fujii, A. Ishitoya, S. Itoh, K. Ozawa, H. Kitaguchi, Improved critical current density in ex situ processed MgB2 tapes by the size reduction of grains and crystallites by high-energy ball milling, Cryogenics (Guildf). 82 (2017) 15–24. https://doi.org/10.1016/j.cryogenics.2017.01.002.

[31] Y. Shimada, S. Hata, K. Ikeda, H. Nakashima, A. Matsumoto, K. Togano, H. Kumakura, Infiltration behavior of molten Mg and its influence on microstructural evolution in SiC-doped MgB2 wires prepared by internal Mg diffusion process, J. Alloys Compd. 740 (2018) 305–311. https://doi.org/10.1016/j.jallcom.2018.01.012.

[32] H. Okamoto, B-Mg (boron-magnesium), J. Phase Equilibria 24 (2003) 92–92. https://doi.org/10.1007/s11669-003-0022-4.

Supplementary Files

This is a list of supplementary files associated with this preprint. Click to download.

- Highlights.docx
- GraphicalAbstract.docx